Modeling of Ungrounded Tangibles on Mutual Capacitance Touch Screens

Christian Bjørge Thoresen and Ulrik Hanke, *Senior Member, IEEE*

***Abstract*—Tangible user interface for touch screens, where interaction happens through tangible objects placed on the screen, is one possible option for addressing the lack of haptic feedback in touch screens. For the development of tangible user interface for mutual capacitance touch screens, it is of interest to be able to model how a tangible on the screen surface is seen by the touch screen controller. Finite Element Method simulations for this case is very demanding in terms of both computational resources and time. In this article, we present a computationally efficient model for simulating the capacitance image of arbitrarily shaped conductive sheets on full size mutual capacitance touch screen panels, with calculation time in the order of milliseconds. Output data from the model show good agreement with corresponding measurement data from experiments, with a root mean square deviation of 1.5% of the peak to peak of the measured values for the modeled screen area.**

***Index Terms*—Mutual capacitance sensing, tangible user interface, touch screen panel.**

I. Introduction

TANGIBLE User Interface (TUI) for touch screens is a field of interest for overcoming the lack of haptic feedback in touch screens. Several examples of TUI for optical rear-camera or light sensitive pixel based touch screens exist [1]. However, these screens are susceptible to interference from ambient light, limiting their use to environments with controlled lighting. TUI for mutual capacitance Touch Screen Panels (TSPs) is therefore an interesting option. Still, mutual capacitance TSPs have typically been designed to detect touches by human fingers, while filtering out other kinds of touches. For this, the TSP makes use of the finger's property of having a strong electrical coupling to the ground potential of the TSP. Thus, touch events can also be triggered by sufficiently ground-coupled, finger-like objects, such as rubber tip styli for TSPs and the TUI touch pads [2], which are both grounded through the user. We have previously demonstrated, both by Finite Element Method (FEM) simulations and experiments, that such TSPs can be enabled to also detect ungrounded conductive objects [3]. This could allow for design of TUI objects that does not rely on grounding through the user or by other means. Detection of ungrounded TUI objects could also be achieved using the modified TSP design presented by Brown et al. [4], which is specifically designed to also be able to detect non-conductive objects by using a different electrode pattern in the digitizer.

This work was supported by The Research Council of Norway, NFR project no 217788.

Christian Bjørge Thoresen and Ulrik Hanke were with respectively the Department of Maritime Operations and the Department of Microsystems at the University of South-Eastern Norway, Campus Vestfold, Raveien 215, NO-3184 Borre, Norway. E-mail: Christian.Thoresen@usn.no

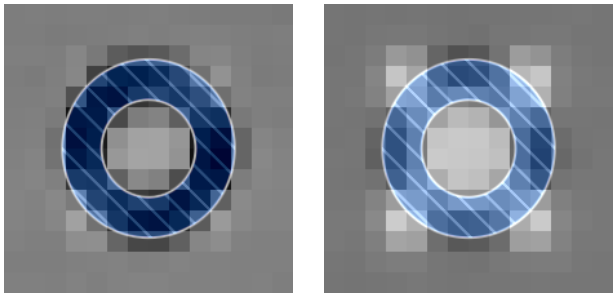

(a) (b)

Fig. 1. Image of the measured raw touch data output for a conductive sheet shaped as the annulus shown overlaid in the images. Dark represents reduction in mutual capacitance, bright represents increase. (a) grounded case, (b) ungrounded case.

A mutual capacitance TSP digitizer consists of an intersecting array of electrodes in the screen surface in the form of rows and columns. The TSP controller works by sampling an image of the mutual capacitances between each pair of intersecting electrodes. This image is influenced by conductive objects as well as variation of permittivity in the proximity of each electrode intersection. Grounded conductive objects, like human fingers, lead to a decrease in mutual capacitance near the object. The capacitance image for a grounded object therefore closely resembles the shape of the screen contact area of the conductive part of the object, as shown in Fig. 1a. This could allow for straight forward application of image registration and interpolation algorithms for determining location and orientation of the object. Ungrounded objects however, may, depending on shape and orientation, lead to various combinations of areas of both increase and decrease in mutual capacitance, as shown in Fig. 1b. This makes it less straight forward to implement algorithms for determining the location and orientation of the object.

Tangibles will typically be differentiated by identification of unique touch patterns contacting the screen. One option is to use different matrix constellations of circular pads, where the center of each pad is determined by regular touch algorithms, as demonstrated for grounded pads [2], [5]. Circular ungrounded pads will give rise to an increase in mutual capacitance in the capacitance image, and similar interpolation algorithms as for grounded touch could be applied to determine the center of the pads. For the TSP design we previously looked at, the sensitivity to such ungrounded circular pads was lower than for grounded pads of the same size [3]. For that TSP, larger pads may be needed for ungrounded operation than for grounded operation. In any case ungrounded

operation would involve modification of the processing of the capacitance image. Then it is also an option to use arbitrarily shaped patterns of conductive material, rather than just a simple pad matrix. This would likely increase the space efficiency of the patterns, allowing more unique patterns of a fixed pattern size or a reduction in the pattern size needed to be able to differentiate a given number of patterns. To achieve this, the detection algorithm will somehow have to take into account the TSP's transformation of the TUI pattern into a capacitance image.

Mutual capacitance TSP controllers may work using different capacitance measurement principles. In this paper we will consider the charge transfer method, where the controller applies a voltage step to one or more Tx-electrode and use charge integrators to measure the amount of charge transfered to each Rx-electrode. This allows for a quasi-static analysis, where we assume that the series resistances can be ignored. We also assume that the controller keeps all of the the Rx-electrodes and all of the inactive Tx-electrodes at constant potential.

The experimental TSP design presented by Brown et al. [4] is able to also detect non-conductive objects by measuring the mutual capacitance to an additional set of Rx-electrodes with different distance to the Tx-electrodes at the intersections. Such a design is also highly applicable to TSPs specialized for tangible detection, as it provides freedom to use the relative permittivity of the materials for designing identification patterns. This can result in a more direct image of the pattern, compared to the use of ungrounded conductive patterns. However, it also requires both a more thorough redesign of both the TSP digitizer, as well as additional channels on a customized TSP controller.

For developing both TUI touch patterns and their detection algorithms, we see the need for an efficient way of modeling the TSP capacitance image output for any given touch pattern. Our previous use of FEM simulations was limited to 5 by 5 TSP electrodes, typically corresponding to about $25\,\mathrm{mm} \times 25\,\mathrm{mm}$ of screen area [3]. These simulations were run on a high end workstation, and each took in the order of $10\,\mathrm{min}$ to complete. For the higher number of electrodes required for the area covered by a TUI identification pattern, these simulations would require access to a computation cluster and become even more time consuming. This cost limits their applicability in development, testing and numerical optimization based tuning of different combinations of patterns and detection algorithms.

With this in mind, we have developed a computationally simple model for mutual capacitance TSPs that calculate the capacitance images for arbitrarily shaped ungrounded conductive sheets on the TSP surface. The model is described in detail in section II, with options for handling fringe field, multiple conductive sheets and multiple layers. In section III we present experiments for the use of the model for a consumer market tablet TSP device, including tuning of model parameters. The results, with comparison of model output versus TSP output for a set of different shapes, are presented and discussed in section IV.

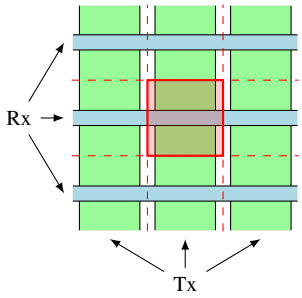

Fig. 2. Top-down view of the Manhattan electrode layout for a section of the screen of 3 by 3 electrodes. The intersection area of the middle Tx- and Rx-electrode is highlighted.

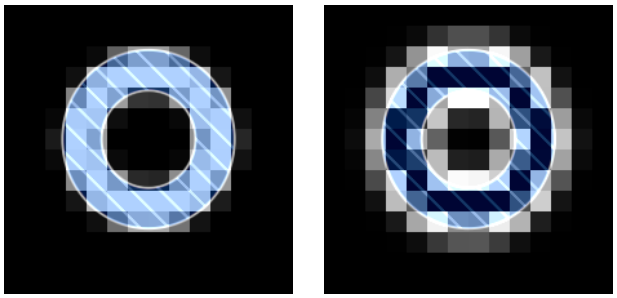

(a) (b)

Fig. 3. Image of the coverage matrix $\mathbf{P}$ (a) and the fringe field matrix $\mathbf{F}$ (b) derived from $\mathbf{P}$ for the annulus shape shown in transparent overlay.

II. The Model

The basic idea of the model is to consider each electrode intersection in the TSP independently. For a mutual capacitance TSP, the screen surface can be divided into a matrix of electrode intersection areas. One such area is highlighted in Fig. 2. From the shape, position and rotation of the conductive pad on the TSP, we determine how large portion of each of these intersection areas that are covered by the pad. This corresponds to a low resolution bitmap image of the conductive pad, with pixel value 0 for no coverage and 1 for full coverage. For a TSP consisting of m Rx-electrodes and n Tx-electrodes, we let the matrix element P_{ij} represent the pad coverage of the intersection area of Rx-electrode i and Tx-electrode j. This results in a coverage matrix $\mathbf{P}$, as shown for an annulus in Fig. 3a.

For our model, we define some parameters to calculate the mutual capacitance reading from this coverage image, illustrated for the case of no coverage and full coverage in Fig. 4. First, for zero coverage, we have the direct mutual capacitance for one electrode intersection in untouched condition, C_0. The presence of a conductive object on the TSP surface above one of the electrode intersection leads to a reduction in the direct mutual capacitance between the two intersecting electrodes. We denote the direct mutual capacitance in the fully covered case as C_0' and define $\Delta C' = C_0' - C_0$.

For the case of a grounded pad, we can then simply model the change in the capacitance image from untouched state as proportional to the coverage matrix $\mathbf{P}$, by expressing the capacitance change matrix $\mathbf{\Delta C'}$ as

$$\mathbf{\Delta C'} = \Delta C' \mathbf{P}. \tag{1}$$

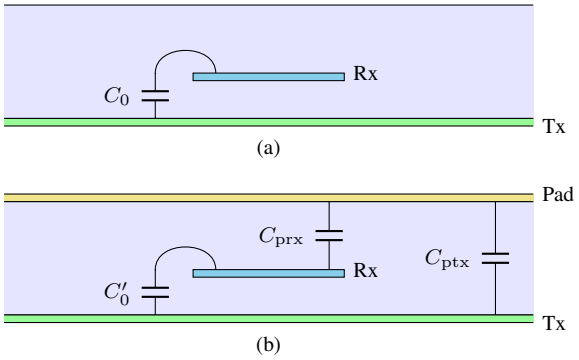

Fig. 4. Cross-section illustration of the capacitances in the electrode intersection without (a) and with (b) a conductive pad covering the area.

For the case of an ungrounded pad, we also have the same reduction in the direct mutual capacitance between intersecting electrodes. However, the ungrounded pad also provides a coupling between all the electrodes it covers. We consider the ungrounded pad as a floating electrode in a multi-electrode capacitor, as illustrated in the circuit diagram in Fig. 5. When the controller applies a voltage to one Tx-electrode, keeping all other electrodes at ground potential, it results in a shift of the floating potential of the pad. The pad can be considered the middle node in a capacitive voltage divider. To find this potential shift, we need the mutual capacitances between the pad and each of the Tx- and Rx-electrodes. Looking at just one electrode intersection area, we define the contribution to the Tx-electrode to pad mutual capacitance from this area as C_{ptx} for a fully covered area, see Fig. 4. Likewise, we have C_{prx} for the Rx-electrode. For a partially covered area, with coverage P_{ij}, the mutual capacitances between the pad and respectively the Tx-electrode and the Rx-electrode can be approximated as $P_{ij}C_{\mathrm{ptx}}$ and $P_{ij}C_{\mathrm{prx}}$. This is shown in Fig. 5, where also the direct mutual capacitance between the electrodes is included as $C_0 + \Delta C' P_{ij}$.

For each Tx-electrode j, we calculate the total mutual capacitance with the pad as the sum of the contributions from each intersection area as

$$C_j^{\mathrm{tx}} = C_{\mathrm{ptx}} \sum_{i=1}^{m} P_{ij}, \qquad j = 1, 2, \ldots, n. \tag{2}$$

Similarly, for each Rx-electrode i, we have

$$C_i^{\mathrm{rx}} = C_{\mathrm{prx}} \sum_{j=1}^{n} P_{ij}, \qquad i = 1, 2, \ldots, m. \tag{3}$$

Applying a voltage V_0 to Tx-electrode l, considering all the other screen electrodes to be kept at ground potential, we model the the pad to ground capacitance as

$$C_l^{\mathrm{gnd}} = C_{\mathrm{pe}} - C_l^{\mathrm{tx}}, \tag{4}$$

where C_{pe} is the total pad to electrodes capacitance,

$$C_{\mathrm{pe}} = \sum_{i=1}^{m} C_i^{\mathrm{rx}} + \sum_{j=1}^{n} C_j^{\mathrm{tx}}. \tag{5}$$

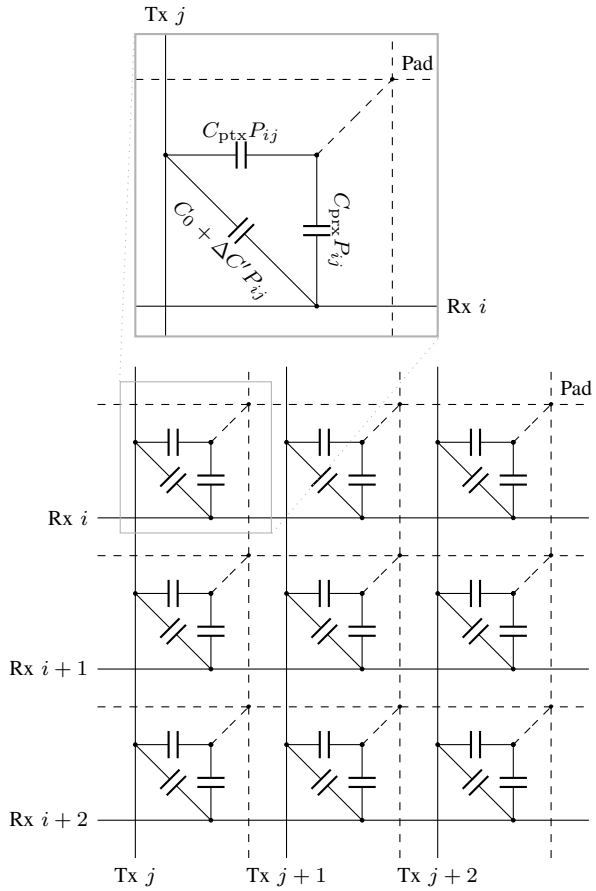

Fig. 5. Circuit diagram for a 3 by 3 electrode sub-section of the digitizer as used in the simplest model for ungrounded pads. The capacitance values are given in terms of the relative pad coverage for the intersection area, P_{ij}. The dashed lines represent the conductive pad, with varying capacitive coupling to the different parts of the electrodes.

The potential shift of the floating pad due to the voltage applied to Tx-electrode l is then given by a capacitive voltage divider as

$$\Delta V_l^{\mathrm{pad}} = V_0 \frac{C_l^{\mathrm{tx}}}{C_l^{\mathrm{gnd}} + C_l^{\mathrm{tx}}} = V_0 \frac{C_l^{\mathrm{tx}}}{C_{\mathrm{pe}}}. \tag{6}$$

This potential shift of the pad due to Tx-electrode l results in a change in the charge on Rx-electrode k

$$\Delta Q_{kl}^{\mathrm{rx}} = -\Delta V_l^{\mathrm{pad}} C_k^{\mathrm{rx}} = -V_0 \frac{C_k^{\mathrm{rx}} C_l^{\mathrm{tx}}}{C_{\mathrm{pe}}}. \tag{7}$$

With this charge, we calculate the capacitance contributed by the ungrounded pad to the total Tx- to Rx-electrode capacitance measured by the TSP controller as

$$\Delta C_{kl}^{\mathrm{txrx}} = \frac{\Delta Q_{kl}^{\mathrm{pad}}}{-V_0} = \frac{C_k^{\mathrm{rx}} C_l^{\mathrm{tx}}}{C_{\mathrm{pe}}}. \tag{8}$$

Substituting (2), (3) and (5) into (8), we obtain

$$\Delta C_{kl}^{\mathrm{txrx}} = \frac{C_{\mathrm{prx}} C_{\mathrm{ptx}}}{(C_{\mathrm{prx}} + C_{\mathrm{ptx}})} \frac{\left(\sum_{j=1}^{n} P_{kj}\right)\left(\sum_{i=1}^{m} P_{il}\right)}{\sum_{i=1}^{m}\sum_{j=1}^{n} P_{ij}}. \tag{9}$$

We combine the two pad to electrode capacitance parameters C_{prx} and C_{ptx} into a new parameter C_{ptr}, corresponding to the series capacitance of the two:

$$C_{\mathrm{ptr}} = \frac{C_{\mathrm{prx}} C_{\mathrm{ptx}}}{C_{\mathrm{prx}} + C_{\mathrm{ptx}}} \tag{10}$$

$$\Delta C_{kl}^{\mathrm{txrx}} = C_{\mathrm{ptr}} \frac{\left(\sum_{j=1}^{n} P_{kj}\right)\left(\sum_{i=1}^{m} P_{il}\right)}{\sum_{i=1}^{m}\sum_{j=1}^{n} P_{ij}} \tag{11}$$

On matrix form, the numerator can be expressed as the outer product of the row sum and column sum vectors of the coverage matrix. By combining this positive capacitance contribution with the negative contribution due to reduction of the direct mutual capacitance (1), we can express the total change in measured capacitance as

$$\Delta C_{kl}^{*} = \Delta C' P_{kl} + \Delta C_{kl}^{\mathrm{txrx}}. \tag{12}$$

A. Tx-Electrode Drive Sequence

The one by one activation of Tx-electrodes described so far does not apply to all TSPs. By oscilloscope measurements on small aluminum pads put on the screen, we found that the tablet TSP used in our experiments activates Tx-electrodes in neighboring pairs, with overlap. Each Tx-electrode is activated twice in a complete scan, except for the first and last electrode. Each point in the data obtained from the controller represent the capacitance between two adjacent Tx-electrodes and one Rx-electrode. This can easily be adjusted for in the model by letting $C_l^{\mathrm{tx}'}$ represent the total pad to active group of Tx-electrode capacitance, in this case simply $C_l^{\mathrm{tx}'} = C_l^{\mathrm{tx}} + C_{l+1}^{\mathrm{tx}}$. We then replace the occurrences of C_l^{tx} with $C_l^{\mathrm{tx}'}$ in the numerator in (8). The model can be adapted to other Tx-electrode drive patterns in a similar way.

B. Fringe Field Contribution

So far we have considered the capacitance to be proportional to the overlap only, as in a parallel plate capacitor simplification. There is also an electric fringe field from the electrode area close to, but not covered by the pad, between the electrodes and the edges and top surface of the pad. One way to include this field in the model is to generate a fringe field matrix similar to the coverage matrix, but describing the areas affected by fringe field instead. Then the fringe field capacitance contribution can be expressed as a function of this matrix and included in the model.

There are several possible ways to generate such a fringe field matrix from the coverage matrix. Considering these matrices as images, we can apply regular image processing techniques. A very simple approach is to first apply Gaussian blur to the coverage matrix, as this results in positive values also for the areas adjacent to the pad. The standard deviations of the Gaussian blur σ_{x}, σ_{y} can be used as a parameter to control how the values should depend on distance from the pad. However, this image also includes the contribution from the area covered by the pad, whereas we only desire an image of a halo around the pad. We achieve this by using the coverage matrix as a mask, by calculating the Hadamard (element wise) product of the blurred $\mathbf{P}$ and the mask $1 - \mathbf{P}$. We denote the resulting fringe field matrix as $\mathbf{F}$. An example is shown in Fig. 3b.

In the model we modify equations (1), (2) and (3) to all include a contribution from this fringe field matrix.

$$\mathbf{\Delta C'} = \Delta C' \left(\mathbf{P} + k_{\mathrm{rxtx}}\mathbf{F}\right) \tag{13}$$

$$C_l^{\mathrm{tx}} = C_{\mathrm{ptx}} \sum_{i=1}^{m} \left(P_{il} + k_{\mathrm{ptx}} f_{il}\right) \tag{14}$$

$$C_k^{\mathrm{rx}} = C_{\mathrm{prx}} \sum_{j=1}^{n} \left(P_{kj} + k_{\mathrm{prx}} f_{kj}\right) \tag{15}$$

Here k_{rxtx}, k_{txp} and k_{rxp} are parameters representing the relative contribution of the fringe field matrix to the different capacitances. In addition we have chosen to have only one parameter for the Gaussian blur, $\sigma_{\mathrm{g}} = \sigma_{\mathrm{x}} = \sigma_{\mathrm{y}}$.

For the non-fringe model, we combined C_{ptx} and C_{prx} into one parameter, C_{ptr}. It is possible to show that it can be used as a good approximation also for this fringe model when $k_{\mathrm{ptx}} \approx k_{\mathrm{prx}}$ or when the contribution from the fringe field to C_{pe} is small.

C. Multiple Pads

Putting multiple isolated pads on each tangible may be useful for creating uniquely identifiable patterns, in the same manner as this has previously been used with grounded pads [2]. Being able to simulate unconnected pads is also useful for the case of analyzing possible interaction between tangibles in close proximity. If we make the assumption that the direct pad to pad capacitance is negligible, we can easily extend the model to work for multiple pads. As input, we need to have one coverage matrix $\mathbf{P}_q$ for each of the n_{p} individual pads. We then apply (1) to the sum of all the individual coverage matrices, whereas we calculate the positive capacitance change contributions (8) individually for each pad and sum them,

$$\Delta C_{ik}^{*} = \Delta C' \sum_{q=1}^{n_{\mathrm{p}}} \left(P_{q,ik} + \Delta C_{q,ik}^{\mathrm{txrx}}\right). \tag{16}$$

D. Multiple Conductive Layers

The model can be extended to deal with several layers of interconnected conductive shapes above the TSP. This allows for simulation of tangible designs such as the tangible markers described in [6]. These are ungrounded tangibles that are able to trigger regular touch points by providing a capacitive coupling to ground through the TSP panel. Being able to efficiently simulate such tangibles, we may be able to optimize their design for more reliable operation. For this extension of the model we can make use of one set of the parameters $\Delta C'$, C_{ptx} and C_{prx} for each layer, as well as having one coverage matrix $\mathbf{P}$ for each layer as input.

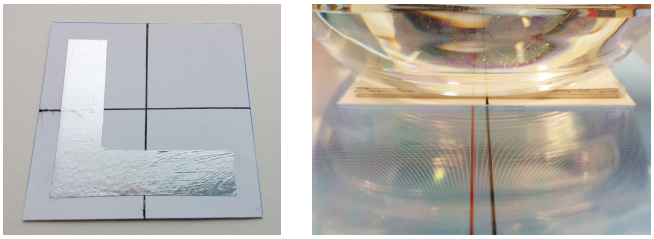

(a) (b)

Fig. 6. Experimental setup, (a) aluminum tape cut to shape and stuck on cardboard, (b) side view of the cardboard piece with the aluminum tape facing down, aligned and weighted down using 4 layers of cardboard and an empty glass.

E. Sub-Pixels

So far we have assumed uniform capacitance contribution from the pad over the entire electrode intersection area. Considering the electrode structure shown in Fig. 2, we would expect the pad area overlapping the Rx-electrode to have increased contribution to C^{rx} and reduced contribution to C^{tx} compared to the area only overlapping the Tx-electrode. To account for non-uniform capacitance contributions over the intersection area, we can divide each intersection area into n_{s} by n_{s} smaller areas. The model parameters $\Delta C'$, C_{prx} and C_{ptx} then become n_{s} by n_{s} matrices to be multiplied element wise with sub-matrices from a coverage matrix with resolution increased a factor n_{s} in each direction. A similar approach is to derive three different coverage matrices from the model input, one for the Rx-electrode coverage, one for the Tx-electrode coverage and one for the contribution to direct reduction in mutual capacitance.

F. Model Implementation

For implementing and testing the model, we have used Python (3.5.1) scripting with the Numpy (1.10.4) package for matrices and Scipy (0.17.0) for statistics and optimization. For drawing the shapes to create the coverage matrices, we used the python package Skimage (0.11.3). The drawing functions, as we used them, render the shapes as pixels of value 0 or 1. Rendering directly to the coverage matrix would then lead to considerable error at the edges of the shapes due to spatial aliasing. We therefore used an oversampling of 16 by 16 pixels for each element in $\mathbf{P}$. This still leads to an inaccuracy of the coverage matrix at the edges of the shapes of up to a value of $1/32$ or $3.3\,\%$.

III. Experiment

We cut ten different shapes from a sheet of aluminum tape by hand and stuck them to $5\,\mathrm{cm} \times 5\,\mathrm{cm}$ pieces of cardboard ($0.4\,\mathrm{mm}$ thick), see Fig. 6a, for testing on a Samsung Galaxy Note 10.1 (GT-N8010) tablet device. For this device we can retrieve raw touch data as a matrix [3]. The center axes of the shapes were marked on the back of each piece of cardboard, including $45°$ rotation for some of the samples. For aligning the samples, the tablet was set to display two cross-hairs, one marking the location of the center of a touch pixel in the middle of the screen and one marking the common corner of 4 adjacent touch pixels. This allowed us to align the pieces for symmetry around one center pixel or for symmetry around a pixel intersection.

The cardboard pieces with the aluminum tape shapes were weighted down by a stack of 4 additional cardboard pieces stuck to the flat bottom of an empty glass, to achieve even pressure, as shown in Fig. 6b. This setup is expected to increase the fringe field to the back surface of the aluminum tape making up the shapes, as the relative permittivity of the volume above the shape (cardboard and glass) is increased compared to air. However, this is similar to the practical use case where a tangible object has conductive shape adhered to its base surface that is in contact with the TSP. For each shape and rotation we acquired 3 capacitance images for each of the two different alignments, for a total of $16 \times 2 \times 3$ capacitance images. The full set of shapes and rotations used is shown in Fig. 7.

We also calculated the corresponding capacitance images for each sample using our model. To reduce the effect of inaccuracies in our manual alignment, we used cross correlation based image registration [7] to find an approximation of how much the sampled images were translated compared to the modeled images. We then recalculated the modeled capacitance images with new coverage matrices based on the translations found. This does however not account for rotation error. The position correction data for all samples had a root mean square (RMS) value of $0.6\,\mathrm{mm}$ and a maximum of $1.6\,\mathrm{mm}$. From the full screen area, we extracted an area of 14 by 14 touch pixels centered at the shape for the comparison of experimental and modeled data. This corresponds to an area of $7\,\mathrm{cm} \times 7\,\mathrm{cm}$. With this size there is sufficient margin to ensure that all touch pixels influenced by the shape are within the area. As a measure of how well the model fits the experimental data, we calculated the Pearson correlation coefficient and the root mean square deviation (RMSD).

A. Determining Model Parameters

We applied two different strategies in order to determine the model parameters, FEM simulation and numerical optimization based on experimental data. For the FEM simulations, we used the same FEM setup as described in [3], with the same TSP parameters. A 3 by 3 electrode simulation is sufficient for the simplest form of the model, where only the middle electrodes are considered. For determining C'_0, C_{ptx} and C_{prx}, we covered the entire TSP surface by a grounded conductor in the simulation. This corresponds to the case of a large pad covering the entire TSP-surface, thereby eliminating the fringe field to the back side of the pad. For C_{ptx} and C_{prx}, we in turn applied a voltage respectively to the middle Tx-electrode and to the middle Rx-electrode. From those simulations, the corresponding capacitances were found from the resulting charge on the the area of the grounded conductor corresponding to only the middle electrode intersection area, as shown in Fig. 2. In the same simulation setup, corresponding to fully grounded touch, C'_0 was found as the capacitance between the two middle electrodes. In order to determine C_0, we used a simulation with only air above the TSP-surface and no conductive pad, corresponding to the untouched state.

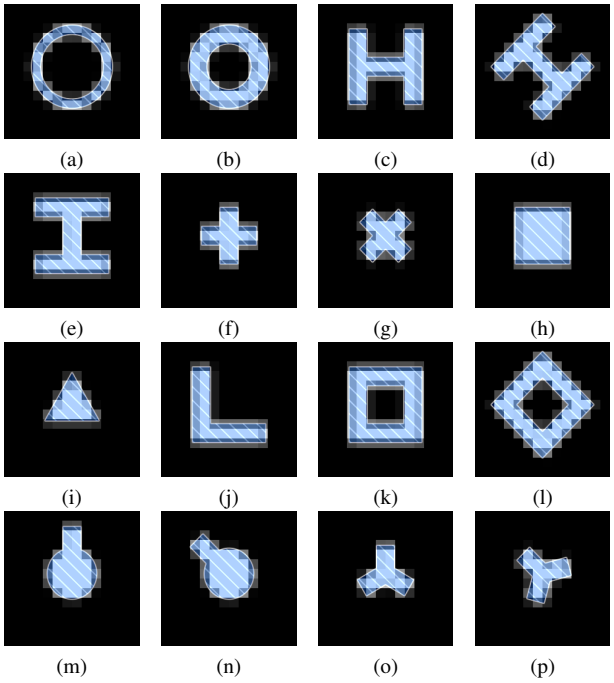

Fig. 7. Outlines of the different shapes and their orientations as used in the experiments, overlaid over the corresponding input to the touch model.

For numerical optimization we used the Pearson distance, $1-r$, as a cost function, where r is the Pearson correlation coefficient between experimental data and corresponding model data. The simple model can be described by two parameters, $\Delta C'$ and C_{ptr} (10). When not considering the scale of the model output, as is the case with the chosen cost function, we can only determine the ratio between these two parameters. We therefore fixed the value of $\Delta C'$ to the one found in the FEM simulations, leaving only one parameter to be determined. For the fringe model, there are four additional parameters to determine, k_{ptx}, k_{prx}, k_{rxtx}, and σ_{g}.

For parameter optimization, we used the bound constrained quasi-Newton method by Broyden, Fletcher, Goldfarb, and Shanno, as implemented in the Python package SciPy [8]. We constrained all parameters to positive non-zero values. Using the scale insensitive Pearson correlation coefficient as a measure of fit, we still need to scale the model output to match the count values from the TSP. For the model to have a correct zero-output for the large screen area not covered by any conductive sheet, we used a least squares fit for scale factor only, with no offset.

IV. Results and Discussion

The model parameters found by FEM and parameter optimizations are listed in Table I, along with the results of comparing the output of the different models with measurement data from all of the measurements. Models A and B are both non-fringe models, where A is based on FEM and B is based on parameter fitting using numerical optimization. We see that the value for the C_{ptr} parameter calculated from FEM, model A, correspond well with the one found by fitting the model to the data, model B. Models C and D are both fringe-field models. For model C, C_{ptx} and C_{prx} are from the FEM simulation, whereas the remaining parameters were fitted. Model D has all parameters fitted. We see a variation in the fringe parameters between these two models. It is worth noting that these parameters are not necessarily completely independent. Although C_{ptr} is used as a parameter in the optimization in model D, the fringe field expression was defined using C_{ptx} and C_{prx}. For this, we have simply used $C_{\mathrm{ptx}} = C_{\mathrm{prx}} = 2C_{\mathrm{ptr}}$ for model D. Furthermore, the σ_{g} parameter does also to some degree influence the overall contribution of the fringe field.

TABLE I
Parameter Values and Results

	Model variants			
Parameter / result	**A**	**B**	**C**	**D**
$\Delta C'$ (pF) [a]	-0.25	-0.25	-0.25	-0.25
C_{ptx} (pF)	0.74		0.74	
C_{prx} (pF)	0.62		0.62	
C_{ptr} (pF)	0.34[b]	0.32	0.34[a]	0.31
k_{ptx}			0.59	0.78
k_{prx}			0.66	0.64
k_{rxtx}			0.97	0.76
σ_{g}			0.37	0.50
Correlation coefficient	0.967	0.972	0.980	0.984
RMSD (count)	29.3	28.6	24.2	21.9
Residuals mean (count)	-4.5	-9.3	-7.6	-8.8
Residuals std.dev (count)	28.9	27.1	23.0	20.1
LSQ scale factor (fF/count)	0.77	0.71	0.80	0.72

[a] Fixed for all model variants, based on FEM simulations.
[b] Calculated values.

Table I also lists the performance results for each of the models. The correlation coefficients for measured and modeled data are higher and the RMSDs are lower for the fitted models compared to the FEM based model. These numbers suggest that model D is superior in simulating the touch screen output, although at a slight increase in computational cost compared to the non-fringe models, A and B. A scatter plot of the residuals for model A and model D is shown in Fig. 8, illustrating how model D has a tighter distribution of residuals over the full range of count values. From the plot, we can also see that the model is more accurate for low or negative count values, where the spread of the residuals is lower than for count values around 400. Expressed in terms of the observed peak to peak value for measured data, the RMSD value for model A is $2.0\,\%$ and for model D it is $1.5\,\%$.

We have used gaussian kernel density estimation to illustrate the distribution of the residuals for the different models in Fig. 8, as well as in Fig. 9. In these graphs we see that the distribution of the residuals, defined as modeled value minus experimental value, has mean values below zero. The mean residual for the two models shown are -4.5 for model A and -8.8 for model D. As mentioned, the cardboard supporting the aluminum tape shapes influences the capacitance image compared to if this volume was filled with air only. This is a likely contribution to the negative mean values of the residuals, as the cardboard increase the capacitance seen in

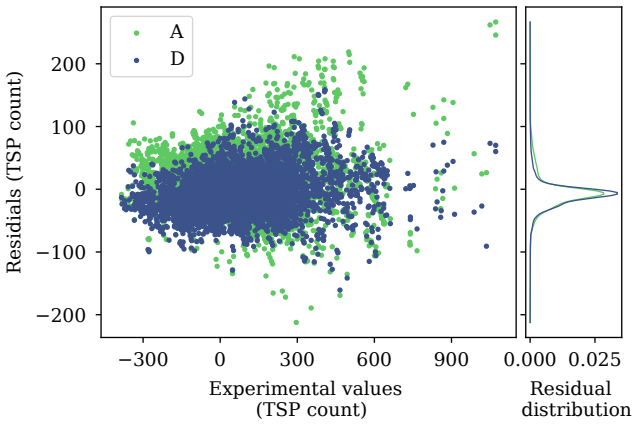

Fig. 8. Scatter plot of residuals from model comparison with all measurements for model A and D. Distributions of the residuals are shown using Gaussian kernel density estimation.

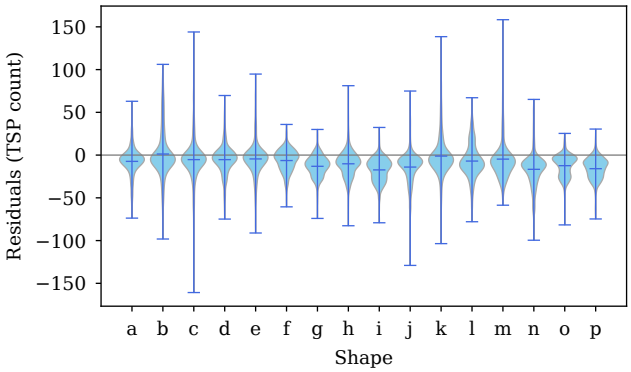

Fig. 9. Violin plot of the residuals for the various shapes for model D, showing means, extrema and distribution of the residuals.

the measurements. To test this, we also acquired data for a plain piece of cardboard, resulting in an average count value of 26 over the cardboard covered area. However, the cardboard only covers part of the sampled area, 10 by 10 points out of a total of 14 by 14. Furthermore, parts of the cardboard area is covered by the conductive shapes. By subtracting the cardboard contribution from the measured TSP data at the points where only the cardboard was covering the screen, we got mean residual values for model A and D of 2.6 and -1.5.

For a practical TUI application with ungrounded pads, the tangible itself, on which the pad is attached, will also likely influence the capacitance image in a similar way. For applications requiring high accuracy, or if the tangible material itself has a high relative permittivity, it may therefore be of interest to also include the effect of the tangible in the model. This could be implemented by modifying the no-touch capacitance and the fringe factors according to a coverage matrix for the area covered by the material of the tangible. One possible application is the detection of presence of liquid in a liquid container tangible, where the liquid above the tag shape will influence the capacitance image.

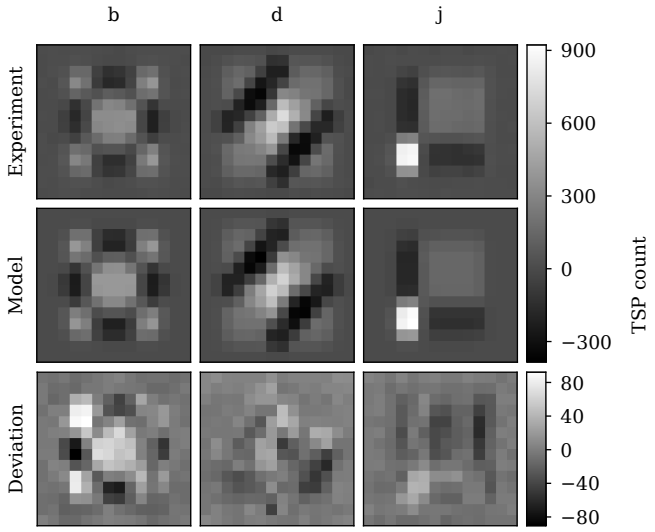

Fig. 10. Comparison of experimental data from the TSP and output from model D for three different shapes (b), (d) and (j). The deviation between model output and measurement is shown in different scale.

Fig. 10 shows a side by side comparison of measurement data and data from model D for the recurring annulus shape (b) and two other shapes, as well as the difference between the measured and modeled data. The comparison clearly shows the ability of the model to simulate an easily recognizable capacitance image. For these three samples, the one from shape (b) stands out as least accurate. Part of the deviation can be attributed to the differences between model inputs and the geometry of the hand cut shapes. A local geometry error of $0.5\,\mathrm{mm}$ could lead to a $10\,\%$ error in the coverage matrix elements. Also, the capacitance contribution is not uniform across the intersection area, leading to some degree of rasterization issues. The proposed sub-pixel extension could improve on the deviation due to rasterization.

In the experiments of ungrounded touch, we observed count values from the TSP device in the range -380 to 1070. For the circular pads we studied in [3], we observed count values in the range of -600 to 360 for respectively grounded and ungrounded touch conditions. In terms of the capacitance reduction previously observed for regular grounded touch, the results presented here are $63\,\%$ for capacitance reduction and $180\,\%$ for capacitance increase. This suggests that specially crafted conductive shapes may be used to induce capacitance reductions sufficient to trigger grounded touch events in regular TSP controllers, as was demonstrated for the multilayer tag in [6]. We also have the option of inducing even stronger increases in capacitance, which can be detected by customized TSP controllers. From the experiments here, one example of a shape with strong capacitance increase is the L-shape (j), shown in Fig. 10, where there is a strong increase in capacitance at the corner of the L. However, this peak is only seen when the L is aligned with the TSP electrodes, as the capacitance image is highly orientation dependent. It is therefore difficult to design patterns that consistently gives rise to increase or decrease in capacitance independent of orientation. Having access to an efficient simulation tool may

TABLE II
HOLDOUT TESTS

Test set	RMSD holdout	RMSD no holdout
(a) - (d)	22.4	22.4
(e) - (h)	18.8	18.4
(i) - (l)	22.9	22.9
(m) - (p)	23.7	23.6

allow the use of numerical optimization for aiding in the attempt of designing such patterns.

To test for overfitting, we divided the samples into four sets, (a)-(d), (e)-(h), (i)-(l), and (m)-(p), and cycled through all, holding one set out as a test set while using the three other sets for the parameter fitting of model D. The resulting RMSD values for each test set, both when it is held out from the training set and not, are shown in Table II. The small differences between holding each set out or not show that the model works well with shapes not included in the training set.

V. FUTURE WORK

For future work we suggest applying the model in design of TUI for mutual capacitance touch screens, as this was the intended application of the model when developing it. This involves using it for designing both uniquely identifiable patterns and corresponding detection algorithms. One possibility is to make use of the model in reverse in such an algorithm, that is to determine the shape of the conductive sheet, given the capacitance image. This may prove useful, as one can then apply image registration with rotation to determine the position and orientation of the tangible. Other future work includes improving on the suggested extensions to the model, such as multiple pads, multiple conductive layers and subpixel treatment of the capacitance contributions. It may also be interesting to look into modeling the effect of the permittivity of non-conductive materials, possibly for also modeling the TSP design by Brown et al. [4]. For a complete TUI on TSP system, it may also be of interest to apply this model for adjustment of the balance between sensitivity to grounded and ungrounded touch, by adjustment of the TSP digitizer geometry parameters.

VI. CONCLUSION

We have developed and tested a computationally efficient model for simulation of the capacitance image in mutual capacitance TSPs due to an ungrounded conductive sheet of arbitrary shape. We achieved high correlation between measurements and model output, and the model should be well suited for use in designing TUI identification patterns and their detection algorithms. The use of bitmaps as input for the model makes it flexible in use. For a TSP panel with known design parameters, we demonstrated using both FEM and parameter fitting to determine model parameters. The FEM based model can be useful to see the influence different TSP-parameters has on the capacitance images when designing a TSP. Parameter fitting is useful for modeling an existing TSP with possibly unknown design parameters, using measurements of a set of test shapes to determine the model parameters.

REFERENCES

[1] S. Jordà, G. Geiger, M. Alonso, and M. Kaltenbrunner, "The reacTable: Exploring the synergy between live music performance and tabletop tangible interfaces," in *Proc. TEI '07*, Baton Rouge, LA: ACM, 2007, pp. 139–146.

[2] T. Götzelmann and D. Schneider, "CapCodes: Capacitive 3D printable identification and on-screen tracking for tangible interaction," in *Proc. NordiCHI '16*, Gothenburg, Sweden: ACM, 2016, 32:1–32:4.

[3] C. B. Thoresen and U. Hanke, "Numerical Simulation of Mutual Capacitance Touch Screens for Ungrounded Objects," *IEEE Sensors Journal*, vol. 17, no. 16, pp. 5143–5152, Aug. 2017.

[4] C. Brown, A. Kay, Y. Sugita, and K. Kida, "60.1: Distinguished Paper: A Capacitive Touch Panel for Simultaneous Detection of Non-Conductive and Conductive Objects," *SID Symposium Digest of Technical Papers*, vol. 46, no. 1, pp. 891–894, Jun. 2015.

[5] N. H. Yu, L. W. Chan, S. Y. Lau, S. S. Tsai, I. Hsiao, D. J. Tsai, F. I. Hsiao, L. P. Cheng, M. Chen, and P. Huang, "TUIC: Enabling tangible interaction on capacitive multi-touch displays," in *Proc. CHI '11*, Vancouver, BC, Canada: ACM, 2011, pp. 2995–3004.

[6] S. Voelker, K. Nakajima, C. Thoresen, Y. Itoh, K. I. Øvergård, and J. Borchers, "PUCs: Detecting transparent, passive untouched capacitive widgets on unmodified multi-touch displays," in *Proc. ITS '15*, St. Andrews, Scotland: ACM, 2013, pp. 101–104.

[7] M. Guizar-Sicairos, S. T. Thurman, and J. R. Fienup, "Efficient subpixel image registration algorithms," EN, *Optics Letters*, vol. 33, no. 2, pp. 156–158, Jan. 2008.

[8] R. Byrd, P. Lu, J. Nocedal, and C. Zhu, "A Limited Memory Algorithm for Bound Constrained Optimization," *SIAM Journal on Scientific Computing*, vol. 16, no. 5, pp. 1190–1208, Sep. 1995.

Christian Bjørge Thoresen received the B.Sc. degree in electrical engineering from the University of South-Eastern Norway (USN), Kongsberg, in 2008 and the M.Sc. degree in Microsystems technology from USN, Horten, in 2012. He is currently pursuing the Ph.D. degree at USN, Horten. His current interest of research is tangible user interface for capacitive touch screens.

Ulrik Hanke (SM'06) received the Siv.Ing. degree and the Dr.Ing. degree in physics from the Norwegian University of Science and Technology (NTNU), Trondheim, Norway, in 1989 and 1994, respectively. After two years as a Post. Doc. he worked for a decade as a research scientist at department of communication technology, SINTEF. Since 2006, he has been with University of South-Eastern Norway, Horten, where he is a Professor of Micro- and Nanosystem technology. His current main research interests are in theory, design, and modeling of piezoelectric and RF acoustic micro devices.